# Ternary silicides Sclr4Si2 and RERh4Si2 (RE = Sc, Y, Tb-Lu) and quaternary derivatives RERh4Si2-xSnx (RE = Y, Nd, Sm, Gd-Lu) - structure, chemical bonding and solid state NMR spectroscopy

Daniel Vosswinkel, Christopher Benndorf, Hellmut Eckert, Samir F Matar, Rainer Pöttgen

Daniel Voßwinkel, Christopher Benndorf, Hellmut Eckert*, Samir F. Matar and Rainer Pöttgen*

# Ternary silicides $ScIr_4Si_2$ and $RERh_4Si_2$ ($RE$ = Sc, Y, Tb-Lu) and quaternary derivatives $RERh_4Si_{2-x}Sn_x$ ($RE$ = Y, Nd, Sm, Gd-Lu) – structure, chemical bonding, and solid state NMR spectroscopy

DOI 10.1515/zkri-2016-1957
Received May 10, 2016; accepted June 25, 2016; published online July 13, 2016

**Abstract:** The silicides $ScIr_4Si_2$ and $RERh_4Si_2$ ($RE$ = Sc, Y, Tb-Lu) and silicide stannides $RERh_4Si_{2-x}Sn_x$ ($RE$ = Y, Nd, Sm, Gd-Lu) were synthesized from the elements by arc-melting and subsequent annealing. The new compounds crystallize with the orthorhombic $YRh_4Ge_2$ type structure, space group *Pnma*. They were characterized by X-ray powder patterns and several structures were refined from single crystal X-ray diffractometer data. The main structural motifs of this series of silicides are tricapped trigonal prisms formed by the transition metal and rare earth atoms. One of the two crystallographically independent silicon sites allows for formation of solid solutions with tin, exemplarily studied for $ErRh_4Si_{2-x}Sn_x$. Electronic structure calculations reveal strong covalent Rh–Si bonding as the main stability factor. Multinuclear ($^{29}$Si, $^{45}$Sc, and $^{89}$Y) magic-angle spinning (MAS) NMR spectra of the structure representatives with diamagnetic rare-earth elements (Sc, Y, Lu) are found to be consistent with the crystallographic data and specifically confirm the selective substitution of Sn in the Si2 sites in the quaternary compounds $YRh_4SiSn$ and $LuRh_4SiSn$.

**Keywords:** crystal structure; rare earth silicides; silicon-tin substitution; $^{29}$Si, $^{45}$Sc, and $^{89}$Y Solid state NMR spectroscopy.

***Corresponding authors: Hellmut Eckert,** Institut für Physikalische Chemie, Universität Münster, Corrensstrasse 30, 48149 Münster, Germany; and Institute of Physics in Sao Carlos, University of Sao Paulo, Sao Carlos, SP 13560-970, Brazil, E-mail: eckerth@uni-muenster.de; and **Rainer Pöttgen,** Institut für Anorganische und Analytische Chemie, Universität Münster, Corrensstrasse 30, 48149 Münster, Germany, E-mail: pottgen@uni-muenster.de
**Daniel Voßwinkel and Christopher Benndorf:** Institut für Anorganische und Analytische Chemie, Universität Münster, Corrensstrasse 30, 48149 Münster, Germany
**Samir F. Matar:** CNRS, Université de Bordeaux, ICMCB, UPR 9048, F-33600 Pessac, France

## Introduction

The rare earth ($RE$) elements, together with an electron-rich transition metal ($T$) and an element of the 3rd, 4th, or 5th main group (generally abbreviated as $X$) form a huge number of ternary $RE_xT_yX_z$ intermetallic phases [1]. Partial electron transfer from the rare earth elements leads to substantial $T$–$X$ bonding within the polyanionic $[T_yX_z]$ networks. Depending on the composition, these networks can additionally be stabilized through $T$–$T$ and/or $X$–$X$ contacts. Many of these $RE_xT_yX_z$ phases show interesting magnetic and transport properties. The rare earth magnetic ground state can be influenced via substitutions within the polyanionic $[T_yX_z]$ networks. A typical example concerns the solid solution $CeCu_2Si_{2-x}Ge_x$ [2], which shows a transition from the heavy fermion silicide to the antiferromagnetic germanide, while keeping the structure type. Such substitutions can also stabilize certain structures that are not available as ternary ones, e.g. the solid solution $CeRhIn_{4-x}Mg_x$ ($x$ = 0.79 and 0.84) [3] with $LaCoAl_4$ type structure.

Some examples are known with a complete ordering of two different $p$ elements. Typical structures are $Y_3NiAl_3Ge_2$ [4], $Yb_7Co_4InGe_{12}$ [5], or $La_4Mn_2InGe_4$ [6]. The alterations in valence and size lead to different coordination patterns for the aluminum, indium, and germanium atoms. Recently we obtained the quaternary phases $RE_3Rh_9Si_2Sn_3$ ($RE$ = Y, Sm, Gd-Lu) [7] which show full ordering of isovalent silicon and tin. The large difference in size is manifested in distinctly different coordination environments, i.e. a trigonal $Rh_6$ prism for silicon and a distorted square $Rh_8$ prism for tin. The silicon/tin ordering was also supported by $^{29}$Si solid state NMR spectra and $^{119}$Sn Mössbauer spectroscopy.

Herein we report on a new series of silicides $ScIr_4Si_2$, $RERh_4Si_2$ ($RE$ = Sc, Y, Tb-Lu; $YRh_4Ge_2$ type [8], *Pnma*) which contain two crystallographically independent silicon sites. The one with the slightly larger coordination sphere allows for silicon/tin substitution, leading to quaternary

compounds $RERh_4SiSn$ ($RE$ = Y, Nd, Sm, Gd-Lu). Besides crystal chemical details and electronic structure calculations, we present a concise study by $^{29}Si$, $^{45}Sc$ and $^{89}Y$ solid state NMR spectroscopy.

# Experimental

## Synthesis

Starting materials for the synthesis of polycrystalline $ScIr_4Si_2$, $RERh_4Si_2$, $RERh_4SiSn$ and $YRh_4Ge_2$ (for comparative NMR spectroscopic studies) samples were sublimed ingots of the rare earth metals (Smart Elements), rhodium and iridium powder (Heraeus), silicon lumps (Smart Elements), germanium pieces (Chempur) and tin granules (Merck), all with stated purities better than 99.9 %. Initially a well-shaped single crystal of $SmRh_4SiSn$ was found during our phase analytical studies of the series of $RE_3Rh_9Si_2Sn_3$ [7] using bismuth as a non-reactive flux. Based on this discovery, targeted syntheses of the series were performed by melting the elements in an electric arc furnace [9] in an argon atmosphere of about 700 mbar, similar to the series of $RERh_4Ge_2$ [8]. Argon was purified with titanium sponge (900 K), molecular sieves and silica gel.

The ternary silicides were prepared by arc melting ca. 400 mg of the elements in the ideal stoichiometric ratio of $RE$ : Rh : Si = 1 : 4 : 2 with $RE$ = Sc, Y, Tb–Dy. We observed that annealing did not improve the purity of the $RERh_4Si_2$ silicides. Different annealing sequences at temperatures of 870, 1070 or 1370 K for 5 days (samples in sealed evacuated silica ampoules) led to decomposition into $RERh_5Si_3$ silicides ($UCo_5Si_3$ type structure [10–12]).

Instead, we observed that rapid cooling led to higher purity samples. Subsequently the larger ingots were split into parts of about 40 mg which were then arc-melted separately and recombined afterwards. By this procedure, most samples were obtained in X-ray pure form, suitable for solid state NMR spectroscopy. The terbium compound could only be obtained with $TbRh_5Si_3$ as by-product. A sample with gadolinium exclusively showed formation of $GdRh_5Si_3$. With iridium we only obtained $ScIr_4Si_2$. Lutetium and the larger rare earth elements form silicides $RE_5Ir_{19}Si_{12}$ with $Sc_5Co_{19}P_{12}$ type structure [13] which will be communicated in a forthcoming publication.

The initial work on these phases started with the flux-grown $SmRh_4SiSn$ crystal. The $RERh_4SiSn$ ($RE$ = Y, Nd, Sm, Gd – Lu) samples were then obtained in high purity by arc melting followed by annealing in closed tantalum ampoules (sealed in quartz for oxidation protection) at 1470 K for 16 days. All $RERh_4Si_2$ and $RERh_4SiSn$ samples are stable in air over months.

## X-ray diffraction

All polycrystalline $RERh_4Si_2$ and $RERh_4SiSn$ samples were studied by X-ray powder diffraction using the Guinier technique: Nonius FR 552 camera equipped with an image plate system (Fujifilm, BAS-1800), Cu $K\alpha_1$ radiation and α-quartz ($a$ = 491.30, $c$ = 540.46 pm) as an internal standard. The orthorhombic lattice parameters (Tables 1 and 2) were calculated by least-squares refinements. Correct indexing of the patterns was ensured by a comparison with calculated ones [14].

**Tab. 1:** Refined cell parameters for $ScIr_4Si_2$, $RERh_4Si_2$ and $RERh_4SiSn$ ($RE$ = rare earth element) based on *Guinier*-powder data (standard deviations in parentheses).

| Compound | $a$/pm | $b$/pm | $c$/pm | $V$/nm³ |
|---|---|---|---|---|
| $ScIr_4Si_2$ | 1123.2(2) | 402.65(9) | 881.6(2) | 0.3987 |
| $ScRh_4Si_2$ | 1097.0(1) | 403.24(5) | 885.64(8) | 0.3918 |
| $YRh_4Si_2$ | 1117.0(1) | 410.20(6) | 898.7(1) | 0.4118 |
| $TbRh_4Si_2$ | 1120.0(2) | 409.8(1) | 901.1(2) | 0.4136 |
| $DyRh_4Si_2$ | 1119.2(2) | 410.52(8) | 901.3(1) | 0.4141 |
| $HoRh_4Si_2$ | 1116.2(1) | 409.82(5) | 899.0(1) | 0.4112 |
| $ErRh_4Si_2$ | 1113.8(1) | 409.11(5) | 897.0(1) | 0.4087 |
| $TmRh_4Si_2$ | 1112.8(1) | 409.23(6) | 896.2(1) | 0.4081 |
| $YbRh_4Si_2$ | 1110.5(2) | 408.72(7) | 894.7(2) | 0.4061 |
| $LuRh_4Si_2$ | 1108.7(1) | 408.42(5) | 893.58(9) | 0.4046 |
| $YRh_4SiSn$ | 1157.4(2) | 416.46(9) | 926.2(2) | 0.4464 |
| $NdRh_4SiSn$ | 1166.4(2) | 419.83(6) | 938.9(1) | 0.4598 |
| $SmRh_4SiSn$ | 1162.6(4) | 417.7(1) | 933.1(4) | 0.4531 |
| $GdRh_4SiSn$ | 1160.2(4) | 417.3(1) | 930.4(3) | 0.4505 |
| $TbRh_4SiSn$ | 1158.6(3) | 416.5(1) | 928.0(2) | 0.4478 |
| $DyRh_4SiSn$ | 1156.6(3) | 416.0(2) | 928.1(3) | 0.4466 |
| $HoRh_4SiSn$ | 1154.2(3) | 416.1(2) | 925.5(3) | 0.4445 |
| $ErRh_4SiSn$ | 1154.4(3) | 415.5(2) | 924.4(3) | 0.4434 |
| $TmRh_4SiSn$ | 1152.2(2) | 414.59(9) | 923.5(2) | 0.4411 |
| $YbRh_4SiSn$ | 1147.4(2) | 414.3(1) | 921.2(2) | 0.4379 |
| $LuRh_4SiSn$ | 1146.4(2) | 413.59(7) | 920.3(1) | 0.4364 |

**Tab. 2:** Cell parameters (standard deviations are smaller or equal than 0.2 pm), cell volumes and residuals of single crystals of the solid solution $ErRh_4Si_{2-x}Sn_x$.

| Refined composition (single crystal) | $a$/pm | $b$/pm | $c$/pm | $V$/nm³ | $wR2$ for all data | CSD-No. |
|---|---|---|---|---|---|---|
| $ErRh_4Si_2$ | 1113.8 | 409.1 | 897.0 | 0.4087 | 0.0267 | 431256 |
| $ErRh_4Si_{1.89}Sn_{0.11}$ | 1116.6 | 409.8 | 898.7 | 0.4112 | 0.0568 | 431251 |
| $ErRh_4Si_{1.71}Sn_{0.29}$ | 1121.8 | 411.5 | 903.3 | 0.4169 | 0.0476 | 431248 |
| $ErRh_4Si_{1.61}Sn_{0.39}$ | 1126.9 | 412.1 | 907.5 | 0.4214 | 0.0562 | 431250 |
| $ErRh_4Si_{1.43}Sn_{0.57}$ | 1135.0 | 414.1 | 913.5 | 0.4294 | 0.0445 | 431247 |

The crystallographic data of these crystals have been deposited at FIZ Karlsruhe under the listed CSD numbers.

Irregularly-shaped (conchoidal fracture) single crystals were selected from the carefully crushed samples of several silicides as well as the silicide stannides. The small crystal fragments were glued to thin quartz fibers using bees wax and their quality was tested by Laue photographs on a Buerger camera (white molybdenum radiation, image plate technique, Fujifilm, BAS-1800). Intensity data of most crystals were collected at room temperature by use of a Stoe IPDS II diffractometer (graphite monochromatized Mo Kα radiation; oscillation mode). Numerical absorption corrections were applied to the data sets. Some crystals were measured on a Stoe StadiVari diffractometer equipped with a Mo micro focus source and a Pilatus detection system. Due to a Gaussian-shaped profile of the X-ray source scaling was applied along with the numerical absorption corrections. All relevant crystallographic data and details of the data collections and evaluations are listed in Tables 3 and 4.

**Tab. 3:** Crystal structure data and details of the refinements for $ScRh_4Si_2$, $TbRh_4Si_2$, $LuRh_4Si_{1.96}$, and $ScIr_4Si_2$, *Pnma*, Z = 4.

| Empirical formula | $ScRh_4Si_2$ | $TbRh_4Si_2$ | $LuRh_4Si_{1.96}$ | $ScIr_4Si_2$ |
|---|---|---|---|---|
| Formula weight, g mol$^{-1}$ | 512.8 | 626.7 | 641.5 | 870.0 |
| Unit cell dimension, pm | $a$ = 1097.0(1) | $a$ = 1120.0(2) | $a$ = 1108.7(1) | $a$ = 1123.2(2) |
| (Guinier powder data) | $b$ = 403.24(5) | $b$ = 409.8(1) | $b$ = 408.42(5) | $b$ = 402.65(9) |
| | $c$ = 885.64(8) | $c$ = 901.1(2) | $c$ = 893.58(9) | $c$ = 881.6(2) |
| Cell volume, nm$^3$ | $V$ = 0.3918 | $V$ = 0.4136 | $V$ = 0.4046 | $V$ = 0.3987 |
| Calculated density, g cm$^{-3}$ | 8.69 | 10.07 | 10.53 | 14.49 |
| Crystal size, µm$^3$ | 5 × 5 × 40 | 10 × 20 × 20 | 10 × 20 × 70 | 10 × 20 × 60 |
| Transmission ratio (min/max) | 0.668/0.928 | 0.414/0.808 | 0.180/0.213 | 0.047/0.245 |
| Absorption coefficient, mm$^{-1}$ | 18.5 | 32.9 | 40.8 | 135.0 |
| $F$(000), e | 916 | 1092 | 1114 | 1428 |
| θ range for data collection, deg | 3–32 | 3–33 | 3–35 | 3–33 |
| Range in *hkl* | ±16, ±5, ±13 | ±17, ±6, ±13 | ±17, ±6, ±14 | ±17, ±6, ±13 |
| Total no. of reflections | 4828 | 13480 | 13383 | 12594 |
| Independent reflections/$R_{int}$ | 757/0.0690 | 896/0.0489 | 1012/0.0518 | 869/0.0399 |
| Reflections with $I \geq 3\sigma(I)/R_\sigma$ | 447/0.0665 | 663/0.0318 | 920/0.0100 | 742/0.0150 |
| Data/parameters | 757/44 | 896/44 | 1012/45 | 869/44 |
| Goodness-of-fit on $F^2$ | 0.58 | 0.70 | 1.84 | 1.41 |
| $R1/wR2$ for $I \geq 3\sigma(I)$ | 0.0147/0.0259 | 0.0160/0.0276 | 0.0233/0.0539 | 0.0220/0.0466 |
| $R1/wR2$ for all data | 0.0466/0.0326 | 0.0312/0.0313 | 0.0256/0.0543 | 0.0273/0.0473 |
| Extinction coefficient | 84(5) | 58(4) | 285(15) | 303(11) |
| Largest diff. peak/hole, e Å$^{-3}$ | 4.09/–4.23 | 1.24/–1.24 | 2.46/–2.15 | 2.71/–1.73 |

**Tab. 4:** Crystal structure data and details of the refinements for $SmRh_4Si_{1.03}Sn_{0.97}$, $YbRh_4Si_{1.22}Sn_{0.78}$, and $LuRh_4Si_{1.39}Sn_{0.61}$, *Pnma*, Z = 4.

| Empirical formula | $SmRh_4Si_{1.03}Sn_{0.97}$ | $YbRh_4Si_{1.22}Sn_{0.78}$ | $LuRh_4Si_{1.39}Sn_{0.61}$ |
|---|---|---|---|
| Formula weight, g mol$^{-1}$ | 706.2 | 711.8 | 698.0 |
| Unit cell dimension, pm | $a$ = 1163.26(4) | $a$ = 1142.32(5) | $a$ = 1133.04(2) |
| (single crystal data) | $b$ = 418.45(2) | $b$ = 414.21(1) | $b$ = 413.21(4) |
| | $c$ = 934.69(3) | $c$ = 918.70(3) | $c$ = 912.49(6) |
| Cell volume, nm$^3$ | $V$ = 0.4550 | $V$ = 0.4347 | $V$ = 0.4272 |
| Calculated density, g cm$^{-3}$ | 10.31 | 10.88 | 10.85 |
| Crystal size, µm$^3$ | 10 × 20 × 30 | 10 × 15 × 25 | 10 × 40 × 65 |
| Transmission ratio (min/max) | 0.432/0.688 | 0.378/0.866 | 0.155/0.547 |
| Absorption coefficient, mm$^{-1}$ | 32.2 | 40.7 | 41.7 |
| $F$(000), e | 1220 | 1225 | 1204 |
| θ range for data collection, deg | 3–32 | 3–33 | 3–30 |
| Range in *hkl* | 0–17, ±6, ±13 | ±17, ±6, ±14 | 0–15, ±5, ±12 |
| Total no. of reflections | 2789 | 5947 | 2279 |
| Independent reflections/$R_{int}$ | 869/0.0250 | 941/0.0536 | 701/0.0199 |
| Reflections with $I \geq 3\sigma(I)/R_\sigma$ | 647/0.0316 | 744/0.0212 | 611/0.0129 |
| Data/parameters | 869/45 | 941/45 | 701/45 |
| Goodness-of-fit on $F^2$ | 1.23 | 0.93 | 1.13 |
| $R1/wR2$ for $I \geq 3\sigma(I)$ | 0.0238/0.0508 | 0.0154/0.0300 | 0.0159/0.0338 |
| $R1/wR2$ for all data | 0.0351/0.0522 | 0.0280/0.0329 | 0.0213/0.0350 |
| Extinction coefficient | 216(16) | 43(5) | 261(9) |
| Largest diff. peak /hole, e Å$^{-3}$ | 1.84/–1.96 | 1.18/–1.00 | 1.50/–2.07 |

## EDX analysis

The single crystals investigated on the diffractometers were studied by semiquantitative EDX analyses in a Zeiss EVO® MA10 scanning electron microscope in variable pressure mode with the rare earth trifluorides, Sc, Rh, Ir, $SiO_2$, and Sn as standards. The experimentally obtained compositions were close to the ideal values, respectively the refined compositions for the solid solutions. The conchoidal fracture of the crystals prevented a precise determination of the composition. No impurity elements heavier than sodium were detected.

## Electronic structure calculations

Accurate electronic structure and bonding properties are best obtained within the quantum theoretical density functional theory (DFT) [15,

16]. Among the several methods based on DFT, we used in the present investigation the scalar relativistic full potential augmented spherical wave (ASW) method [17, 18]. The generalized gradient approximation GGA [19] scheme was used to account for the DFT exchange-correlation effects. In the minimal ASW basis set, we chose the outermost shells to represent the valence states and the matrix elements were constructed using partial waves up to $l_{max}+1=4$ for *RE*, $l_{max}+1=3$ for Rh and $l_{max}+1=2$ for Si and Sn. Self-consistency was achieved when charge transfers and energy changes between two successive cycles were such as: $\Delta Q < 10^{-8}$ and $\Delta E < 10^{-6}$ eV, respectively. The BZ integrations were performed using the linear tetrahedron method within the irreducible orthorhombic wedge following Blöchl [20].

The relative magnitude of the chemical bonding is obtained based on the overlap population analysis: $S_{ij}$, i and j being two chemical species. The crystal orbital overlap population (COOP) criterion is used [21]. In the plots positive, negative and zero COOP magnitudes indicate bonding, anti-bonding and non-bonding interactions, respectively.

## Solid state MAS NMR spectroscopy

$^{29}$Si, $^{45}$Sc, and $^{89}$Y solid state NMR spectra were recorded with BRUKER DSX 500, BRUKER DSX 400 and BRUKER AVANCE III spectrometers at resonance frequencies of 79.460 and 59.595 MHz ($^{29}$Si), 121.470 MHz ($^{45}$Sc) and 24.496 MHz ($^{89}$Y). MAS NMR spectra were obtained at spinning frequencies between 5 and 28 kHz in conventional $ZrO_2$ or $Si_3N_4$ MAS rotors with diameters of 2.5, 4 and 7 mm. All samples were ground to fine powders and subsequently mixed with powdered dry sodium chloride in an approximate ratio of 1:2–3 to reduce electrical conductivity and density. Tris(trimethylsilyl)silane (TTMSS; $\delta_{iso} = -9.75$ ppm for the dominant peak), scandium chloride (0.1 molar solution in $H_2O$, $\delta_{iso} = 0$ ppm), yttrium nitrate (8 molar solution with 0.25 mol/L iron(III)nitrate in $H_2O$, $\delta_{iso} = -22.8$ ppm) were used as external references. Conventional single pulse and rotor-synchronized $\pi/2 - \tau - \pi - \tau$ spin echo experiments were carried out using the BRUKER Topspin software [22]. All experimental data were analyzed with the Dmfit [23] software and are listed in Table 8.

**Tab. 5:** Atomic coordinates, equivalent isotropic and anisotropic displacement parameters (pm²) for $ScRh_4Si_2$, $LuRh_4Si_{1.96}$ and $ScIr_4Si_2$.

| Atom | *x* | *z* | $U_{11}$ | $U_{22}$ | $U_{33}$ | $U_{13}$ | $U_{eq}$ |
|---|---|---|---|---|---|---|---|
| $ScRh_4Si_2$ | | | | | | | |
| Sc | 0.3241(1) | 0.3586(2) | 62(5) | 52(6) | 70(6) | −24(4) | 61(3) |
| Rh1 | 0.00243(5) | 0.88374(6) | 49(2) | 29(2) | 41(2) | −13(2) | 40(1) |
| Rh2 | 0.76671(5) | 0.80157(6) | 42(2) | 37(2) | 53(2) | 12(2) | 44(1) |
| Rh3 | 0.06155(5) | 0.32893(6) | 45(2) | 38(2) | 28(2) | 2(2) | 37(1) |
| Rh4 | 0.84186(5) | 0.49137(6) | 40(2) | 35(2) | 35(2) | −5(2) | 36(1) |
| Si1 | 0.1379(2) | 0.0876(2) | 37(8) | 41(9) | 37(8) | 3(6) | 38(5) |
| Si2 | 0.5595(2) | 0.8818(2) | 43(8) | 49(9) | 46(7) | 6(7) | 46(5) |
| $TbRh_4Si_2$ | | | | | | | |
| Tb | 0.32458(3) | 0.35118(3) | 134(1) | 132(1) | 128(1) | −10(1) | 131(1) |
| Rh1 | −0.00011(4) | 0.88478(5) | 130(2) | 120(2) | 128(2) | −10(2) | 126(1) |
| Rh2 | 0.76931(4) | 0.81737(5) | 132(2) | 120(2) | 153(2) | −2(2) | 135(1) |
| Rh3 | 0.05902(4) | 0.32684(6) | 130(2) | 134(2) | 122(2) | −5(2) | 129(1) |
| Rh4 | 0.84504(4) | 0.49437(5) | 131(2) | 129(2) | 127(2) | 2(1) | 129(1) |
| Si1 | 0.1360(2) | 0.0880(2) | 120(7) | 139(7) | 116(7) | −7(5) | 125(4) |
| Si2 | 0.5584(2) | 0.8848(2) | 141(7) | 132(7) | 130(8) | 2(5) | 134(4) |
| $LuRh_4Si_{1.96}$ | | | | | | | |
| Lu | 0.32412(3) | 0.35467(3) | 118(1) | 118(1) | 121(1) | −13(1) | 119(1) |
| Rh1 | 0.00159(5) | 0.88413(6) | 115(2) | 105(2) | 111(2) | −10(1) | 111(1) |
| Rh2 | 0.76857(5) | 0.81245(6) | 111(2) | 110(2) | 132(2) | 2(2) | 118(1) |
| Rh3 | 0.05937(5) | 0.32772(5) | 110(2) | 118(2) | 103(2) | −2(1) | 110(1) |
| Rh4 | 0.84347(4) | 0.49377(6) | 111(2) | 110(2) | 110(2) | −3(1) | 111(1) |
| Si1 | 0.1370(2) | 0.0881(2) | 113(7) | 115(7) | 111(7) | 7(6) | 113(4) |
| 0.95(1) Si2 | 0.5592(2) | 0.8833(2) | 101(8) | 111(8) | 105(8) | −1(5) | 106(5) |
| $ScIr_4Si_2$ | | | | | | | |
| Sc | 0.3261(2) | 0.3590(3) | 185(8) | 200(9) | 190(9) | −17(8) | 192(5) |
| Ir1 | 0.00033(4) | 0.88515(5) | 202(2) | 140(2) | 167(2) | −19(2) | 170(1) |
| Ir2 | 0.77036(4) | 0.79785(5) | 186(2) | 153(2) | 186(2) | 21(2) | 175(1) |
| Ir3 | 0.06073(4) | 0.32911(5) | 165(2) | 153(2) | 153(2) | −3(1) | 157(1) |
| Ir4 | 0.84006(4) | 0.49018(5) | 165(2) | 147(2) | 155(2) | −2(1) | 156(1) |
| Si1 | 0.1390(3) | 0.0840(4) | 162(12) | 160(12) | 164(13) | 4(1) | 162(7) |
| Si2 | 0.5649(3) | 0.8789(4) | 183(12) | 166(13) | 168(13) | 3(1) | 172(7) |

$U_{eq}$ is defined as one third of the trace of the orthogonalized $U_{ij}$ tensor. All atoms lie on Wyckoff positions 4*c* (*x* 1/4 *z*), $U_{12} = U_{23} = 0$.

## Structure refinements

All data sets showed primitive orthorhombic lattices and the systematic extinctions were compatible with space group *Pnma*. Isotypy with the germanides $RERh_4Ge_2$ [8] was already evident from the Guinier powder patterns. The atomic parameters of $YRh_4Ge_2$ [8] were taken as starting values and the structures were refined on $F^2$ with Jana2006 [24] with anisotropic displacement parameters for all atoms. In case of the tin-containing compounds the mixed Sn/Si occupancy was refined as a least-squares variable. Of all other crystals, only one silicon site of $LuRh_4Si_{1.96}$ showed tiny defects. The final difference Fourier syntheses revealed no significant residual peaks in both refinements. The positional parameters, interatomic distances (exemplarily for $LuRh_4Si_{1.96}$ and $LuRh_4Si_{1.39}Sn_{0.61}$) and atomic displacement parameters are listed in Tables 5–7. Further information on the structure refinements is available.[1]

## Crystal chemistry

The silicides $RERh_4Si_2$ (*RE* = Sc, Y, Tb-Lu) are isotypic with the recently reported series of germanides $RERh_4Ge_2$ [8], space group *Pnma*. The cell volumes of the silicides are about 5 % smaller than those of the germanides; a direct consequence of the smaller silicon atoms. The crystal chemical details have been deeply discussed in the original work on the germanide series. In the following discussion we focus on the comparison of the silicide $LuRh_4Si_2$ with its stannide counterpart $LuRh_4SiSn$ (for simplicity we keep the ideal compositions).

A projection of the $LuRh_4Si_2$ structure along the short unit cell axis is presented in Figure 1. Both crystallographically independent silicon sites show slightly distorted trigonal prismatic metal coordination by four rhodium and two lutetium atoms, the typical coordination motif in metal-rich silicides [25]. Two of these trigonal prisms condense to a double unit via a common lutetium edge. Adjacent prismatic double units are shifted by half the *b* translation unit.

Of the two silicon sites only the Si2 one can be substituted by tin. From Table 7 it is already evident that the Si2 atoms have the longer Si2–Rh distances in $LuRh_4Si_2$. Substitution of this leads to a drastic overall increase of the distances of the neighboring atoms (Figure 2). This is a direct consequence of the larger covalent radius of tin (140 pm) when compared with silicon (117 pm) [26]. The enlargement of the trigonal prism also leads to a lengthening of the prism edge (282–307 pm) which corresponds to the Rh3–Rh4 distance. Although tin is a minority component in these quaternary compounds, the cell volumes are about 8 % larger than those for the pure silicides (Table 1). As a consequence of the tin substitution (*X* stands for the Sn/Si mixing) we observe a closer *X*2–*X*2 distance of 327 pm which is within the range of the Sn–Sn distances in β–Sn ($4 \times 302$ and $2 \times 318$ pm) [27] as well as to many ternary rare earth stannides [28], pointing to Sn–Sn bonding. This is addressed in more detail in the chemical bonding section.

An interesting question concerns the existence range for both series. The pure silicides exist only up to terbium as largest rare earth element. The polyanionic network does not leave adequate space for the larger ones. This is different for the quaternary compounds. We observe an overall expansion of the $[Rh_4SiSn]$ network, leaving more space and the $RERh_4SiSn$ series exists up to neodymium.

The lattice parameters within the $RERh_4SiSn$ series decrease almost monotonically from the neodymium to the lutetium compound as expected from the lanthanide contraction. In our early synthesis experiments we repeatedly observed too small cell volumes, which did not fit well into the Iandelli plot. This was due to a too small degree of Si/Sn substitution. We have then exemplarily studied the solid solution $ErRh_4Si_{2-x}Sn_x$ via powder X-ray diffraction and structure refinements of several single crystals with different tin content. The trend of the lattice parameters along with the refined composition (Table 3) is in agreement with Vegard type behavior. Based on these results it is likely that some of the bulk samples might contain a distribution of domains with slightly differing Sn/Si substitution levels.

## Electronic structure and chemical bonding

Starting from the experimental structures (Tables 1–7) for both the silicides and the silicide-stannide, we investigated the electronic structures and bonding properties of the yttrium compounds $YRh_4Si_2$ and $YRh_4SiSn$. The

1 Details may be obtained from: Fachinformationszentrum Karlsruhe, D-76344 Eggenstein-Leopoldshafen (Germany), by quoting the Registry No's. CSD–431254 ($ScRh_4Si_2$), CSD–431257 ($TbRh_4Si_2$), CSD–431255 ($LuRh_4Si_{1.96}$), CSD–431253 ($ScIr_4Si_2$), CSD–431252 ($SmRh_4Si_{1.03}Sn_{0.97}$), CSD–431249 ($YbRh_4Si_{1.22}Sn_{0.78}$), CSD–431246 ($LuRh_4Si_{1.39}Sn_{0.61}$), CSD–431256 ($ErRh_4Si_2$), CSD–431251 ($ErRh_4Si_{1.89}Sn_{0.11}$), CSD–431248 ($ErRh_4Si_{1.71}Sn_{0.29}$), CSD–431250 ($ErRh_4Si_{1.61}Sn_{0.39}$), and CSD–431247 ($ErRh_4Si_{1.43}Sn_{0.57}$).

**Tab. 6:** Atomic coordinates, equivalent isotropic and anisotropic displacement parameters (pm²) for $SmRh_4Si_{1.03}Sn_{0.97}$, $YbRh_4Si_{1.22}Sn_{0.78}$ and $LuRh_4Si_{1.39}Sn_{0.61}$.

| Atom | *x* | *z* | $U_{11}$ | $U_{22}$ | $U_{33}$ | $U_{13}$ | $U_{eq}$ |
|---|---|---|---|---|---|---|---|
| $SmRh_4Si_{1.03}Sn_{0.97}$ | | | | | | | |
| Sm | 0.32515(5) | 0.34914(6) | 83(2) | 74(2) | 78(2) | −8(2) | 78(1) |
| Rh1 | 0.99693(7) | 0.89535(9) | 88(3) | 83(4) | 75(3) | −8(3) | 82(2) |
| Rh2 | 0.77998(7) | 0.81661(9) | 67(3) | 82(4) | 108(4) | 8(3) | 86(2) |
| Rh3 | 0.07045(7) | 0.31645(9) | 85(3) | 70(4) | 84(4) | 7(3) | 80(2) |
| Rh4 | 0.83055(8) | 0.50176(9) | 83(4) | 69(4) | 84(3) | −2(3) | 78(2) |
| Si1 | 0.1346(2) | 0.0838(3) | 60(11) | 17(11) | 55(11) | 1(1) | 44(6) |
| 0.97(1) Sn/0.03(1) Si2 | 0.55830(6) | 0.88512(8) | 65(3) | 57(3) | 64(3) | 1(2) | 62(2) |
| $YbRh_4Si_{1.22}Sn_{0.78}$ | | | | | | | |
| Yb | 0.32438(2) | 0.35373(3) | 77(1) | 54(1) | 73(1) | −14(1) | 68(1) |
| Rh1 | 0.99917(4) | 0.89365(5) | 101(2) | 46(2) | 80(2) | −30(1) | 76(1) |
| Rh2 | 0.77760(4) | 0.81167(5) | 90(2) | 47(2) | 81(2) | 13(2) | 72(1) |
| Rh3 | 0.06844(4) | 0.31958(5) | 114(2) | 92(2) | 65(2) | −13(2) | 90(1) |
| Rh4 | 0.83177(4) | 0.49926(5) | 94(2) | 68(2) | 74(2) | −20(2) | 79(1) |
| Si1 | 0.1357(1) | 0.0851(2) | 71(6) | 45(7) | 76(6) | −4(5) | 64(4) |
| 0.78(1) Sn/0.22(1) Si2 | 0.55906(4) | 0.88272(5) | 58(2) | 42(2) | 53(2) | −1(1) | 51(1) |
| $LuRh_4Si_{1.39}Sn_{0.61}$ | | | | | | | |
| Lu | 0.32388(3) | 0.35485(3) | 91(1) | 64(1) | 85(1) | −14(1) | 80(1) |
| Ir1 | 0.00024(5) | 0.89184(5) | 124(2) | 55(3) | 114(2) | −43(2) | 98(1) |
| Ir2 | 0.77599(5) | 0.81103(6) | 120(2) | 57(3) | 91(2) | 6(2) | 89(1) |
| Ir3 | 0.06569(5) | 0.32179(6) | 136(3) | 126(3) | 86(2) | −23(2) | 116(1) |
| Ir4 | 0.83441(5) | 0.49709(5) | 118(3) | 88(3) | 87(2) | −22(2) | 98(1) |
| Si1 | 0.1360(2) | 0.0868(2) | 93(8) | 59(8) | 76(7) | 1(6) | 76(4) |
| 0.61(1) Sn/0.39(1) Si2 | 0.55909(6) | 0.88227(6) | 79(3) | 49(3) | 65(3) | −1(2) | 64(2) |

$U_{eq}$ is defined as one third of the trace of the orthogonalized $U_{ij}$ tensor. All atoms lie on Wyckoff positions 4*c* (*x* 1/4 *z*), $U_{12} = U_{23} = 0$.

**Tab. 7:** Interatomic distances (pm), for $LuRh_4Si_{1.96}$ (column **A**) and $LuRh_4Si_{1.39}Sn_{0.61}$ (column **B**) calculated with the powder lattice parameters.

| | | | A | B | | | | A | B | | | | A | B |
|---|---|---|---|---|---|---|---|---|---|---|---|---|---|---|
| Lu: | 2 | Rh2 | 273.1 | 280.0 | Rh2: | 1 | *X*2[a] | 240.6 | 254.2 | Rh4: | 1 | *X*1 | 240.3 | 237.5 |
| | 2 | Rh1 | 282.4 | 289.0 | | 2 | *X*1 | 246.1 | 247.6 | | 2 | *X*2[a] | 251.2 | 261.2 |
| | 1 | Rh3 | 294.5 | 294.1 | | 1 | Rh1 | 266.2 | 264.6 | | 1 | *X*2[a] | 263.2 | 277.4 |
| | 2 | *X*1 | 295.1 | 299.2 | | 2 | Lu | 273.1 | 280.0 | | 2 | Rh3 | 280.6 | 287.8 |
| | 1 | Rh2 | 303.8 | 309.7 | | 2 | Rh4 | 288.8 | 295.2 | | 1 | Rh3 | 281.6 | 307.0 |
| | 1 | Rh1 | 305.3 | 305.5 | | 1 | Rh4 | 296.6 | 294.0 | | 2 | Rh2 | 288.8 | 295.2 |
| | 2 | Rh4 | 307.5 | 305.1 | | 1 | Lu | 303.8 | 309.7 | | 1 | Rh2 | 296.6 | 294.0 |
| | 1 | Rh3 | 307.6 | 317.9 | | 2 | Rh3 | 306.2 | 299.3 | | 2 | Lu | 307.5 | 305.1 |
| | 1 | Rh4 | 312.1 | 321.4 | Rh3: | 1 | *X*1 | 230.8 | 228.8 | | 1 | Lu | 312.1 | 321.4 |
| | 1 | *X*1 | 315.9 | 324.3 | | 2 | *X*2[a] | 247.9 | 256.4 | *X*1: | 1 | Rh3 | 230.8 | 228.8 |
| | 2 | *X*2[a] | 322.0 | 327.2 | | 1 | *X*2[a] | 258.2 | 270.1 | | 1 | Rh1 | 236.1 | 235.1 |
| Rh1: | 1 | *X*1 | 236.1 | 235.1 | | 2 | Rh4 | 280.6 | 287.8 | | 1 | Rh4 | 240.3 | 237.5 |
| | 1 | *X*2[a] | 247.4 | 258.9 | | 1 | Rh4 | 281.6 | 307.0 | | 2 | Rh2 | 246.1 | 247.6 |
| | 2 | *X*1 | 256.8 | 258.6 | | 2 | Rh1 | 286.5 | 293.7 | | 2 | Rh1 | 256.8 | 258.6 |
| | 1 | Rh2 | 266.2 | 264.6 | | 1 | Lu | 294.5 | 294.1 | | 2 | Lu | 295.1 | 299.2 |
| | 2 | Lu | 282.4 | 289.0 | | 2 | Rh2 | 306.2 | 299.3 | | 1 | Lu | 315.9 | 324.3 |
| | 2 | Rh3 | 286.5 | 293.7 | | 1 | Lu | 307.6 | 317.9 | *X*2[a]: | 1 | Rh2 | 240.6 | 254.2 |
| | 2 | Rh1 | 290.9 | 285.7 | | | | | | | 1 | Rh1 | 247.4 | 256.4 |
| | 1 | Lu | 305.3 | 305.5 | | | | | | | 2 | Rh3 | 247.9 | 258.9 |
| | | | | | | | | | | | 2 | Rh4 | 251.2 | 261.2 |
| | | | | | | | | | | | 1 | Rh3 | 258.2 | 270.1 |
| | | | | | | | | | | | 1 | Rh4 | 263.2 | 277.4 |
| | | | | | | | | | | | 2 | *X*2[a] | 320.0 | 326.8 |
| | | | | | | | | | | | 2 | Lu | 322.0 | 327.2 |

Standard deviations are equal or smaller than 0.2 pm. All distances of the first coordination spheres are listed.

[a]In the case of $LuRh_4Si_{1.39}Sn_{0.61}$ the *X*2 site is a mixed one with 61 % Sn and 39 % Si.

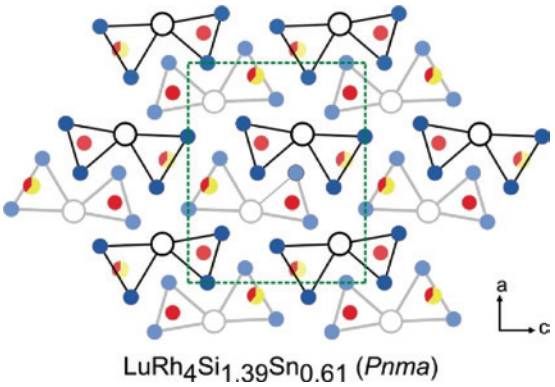


**Fig. 1:** Projection of the $LuRh_4Si_{1.39}Sn_{0.61}$ structure along the short unit cell axis. Lutetium, rhodium, and silicon atoms are drawn in black open, blue, and red color. The mixed occupied Sn/Si site is marked by segments. All atoms are located on mirror planes at $y = 1/4$ (thin lines) and $y = 3/4$ (thick lines). The silicon centered trigonal prisms are emphasized.

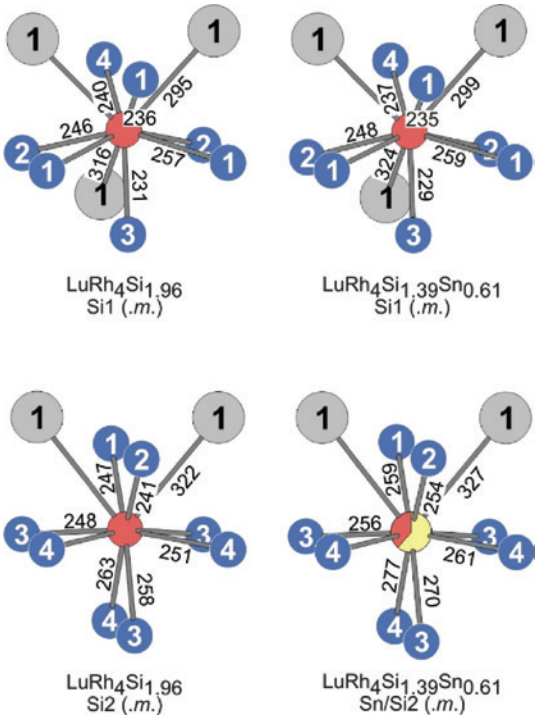


**Fig. 2:** Coordination of the silicon and tin atoms in the crystal structures of $LuRh_4Si_2$ and $LuRh_4Si_{1.39}Sn_{0.61}$. Lutetium, rhodium, and silicon atoms are drawn in medium gray, blue, and red color. The silicon/tin mixing is emphasized by segments. Relevant interatomic distances are given in units of pm.

experimentally refined atomic parameters were checked by preliminary geometry optimization resulting in close agreement. The calculations assume spin degenerate or non-spin polarized (NSP) configuration; in contrast to a spin polarized SP configuration where two spin channels are considered. The latter situation is mainly encountered when the transition element is in the fourth period, as is the case for Fe, Co or Ni, for which the 3*d* states have a more localized character than for the 4*d* or 5*d* transition elements.

The respective site projected densities of states (PDOS) are given in Figure 3 (top) and (bottom). Along the *x*-energy axis the zero-energy is taken with respect to the Fermi level ($E_F$). The two panels show close resemblance especially for the low magnitude DOS at $E_F$ and the splitting of the valence band into *s*-like states from –10 to –8 eV with smaller energy splitting for the silicide-stannide. These electronic structure features are similar to those identified for the germanium compounds $RERh_4Ge_2$ [8].

From –6 eV up to $E_F$, the Rh *d* states are gathered but clearly the large filling of Rh *d* states leads to their presence well within the valence band (VB). The lower part of the *d* block shows significant contributions from Si/Sn *p*-states with similar PDOS shape with Rh *d* belonging to the four different sites. On the contrary, the Y states are seen mainly in the upper part of the *d* block. Yttrium is the first element of the 4*d* series and its little occupied *d* states

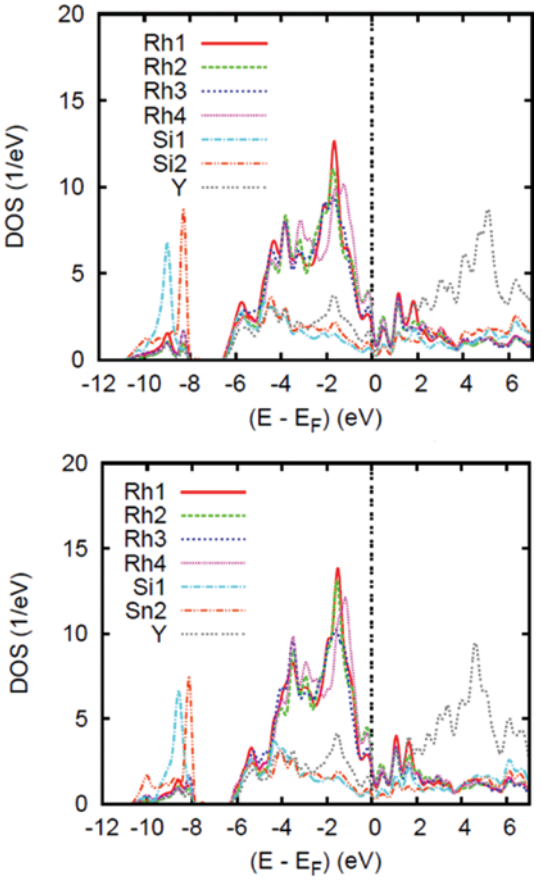


**Fig. 3:** Site projected density of states of $YRh_4Si_2$ (top) and $YRh_4SiSn$ (bottom).

are centered within the conduction band (CB) above $E_F$ so that itinerant Y states are crossing $E_F$. This also applies to states of the other constituent elements, especially the *s* and *p* like states for Si and Sn. Consequently both compounds are expected to be weakly metallic.

Because of the selective occupation of the Si2 sites by Sn, the following discussion will focus on the bonding properties of $YRh_4SiSn$. Figure 4 presents the COOPs for such interactions. In both panels the valence band is of mainly bonding character with positive COOP magnitudes along the *y*-axis. This demonstrates that the stability of the compounds is mainly ensured by the interaction of the Rh substructure with the *p*-element (Si, Sn). It can be noted that the major COOP intensities are in the −6 to −3 eV range. Furthermore, the presence of non-bonding, highly energetic Rh *d* states results in negative (antibonding) COOPs with small amplitudes at the very top of the VB.

We also note that within the energy range $E-E_F < 0$ the COOPs for the four $Rh_i$–Si show similar dependences on energy (Figure 4, top) but they exhibit different intensities with the largest one for Rh1–Si and the smallest intensity for Y–Si. This follows from the respective distances, i.e. the smaller the distance the stronger the bonding. This is less obvious for the interactions with Sn (Figure 4, bottom) where the COOPs for Rh3–Sn and Rh4–Sn show similar intensities whereas Rh1–Sn and Rh2–Sn have much smaller magnitudes; Y–Sn COOPs have vanishingly small intensities. In total, the interaction of the Y and Rh substructures with Sn is much weaker than with Si.

Lastly, we examine the nature of the bonding within the Si/Sn substructure. Figure 5 shows the three different COOPs. Clearly, the Si–Sn interaction is half bonding/half antibonding and therefore does not contribute to the stability of the structure. Si–Si and Sn–Sn bonding also shows such features of compensating positive/negative COOP but more antibonding counterparts are dominant in the case of Sn–Sn. Nevertheless, the major stability of the two compounds is mainly due to the Rh–Si/Rh–Sn bonds.

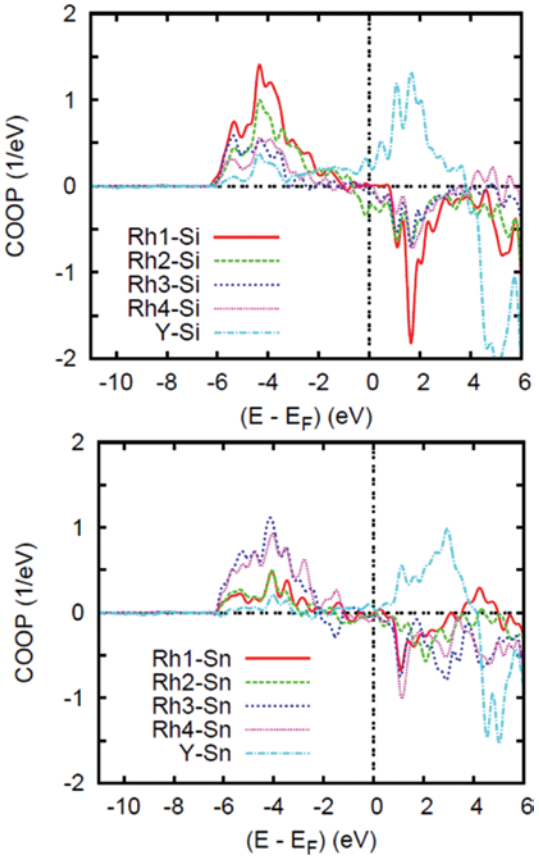


**Fig. 4:** $YRh_4SiSn$: overlap populations within the COOP criterion.

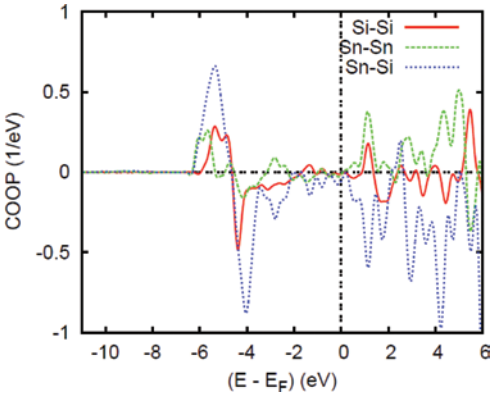


**Fig. 5:** $YRh_4SiSn$: COOP of the *p*-element (Si, Sn) substructures.

## Solid state NMR spectroscopy

The solid state MAS-NMR spectra of the diamagnetic representatives $ScRh_4Si_2$, $ScIr_4Si_2$, $YRh_4Si_2$, $YRh_4Ge_2$, $LuRh_4Si_2$, $YRh_4SiSn$, and $LuRh_4SiSn$ are shown in Figures 6–8. All signals exhibit strong positive resonance shifts caused by the interaction of the nuclear spins with the conduction electron spin density at the Fermi edge, known as Knight Shift. In agreement with the crystal structure of the ternary silicides, the $^{29}Si$ spectra show two distinct signals with an area ratio nearly 1:1 (Figure 6). The unambiguous assignment of these two signals is possible because the substitution of silicon by tin atoms occurs selectively at the Si2 site. In accordance with this fact the $^{29}Si$ spectra of the quaternary compounds $RERh_4SiSn$ show only

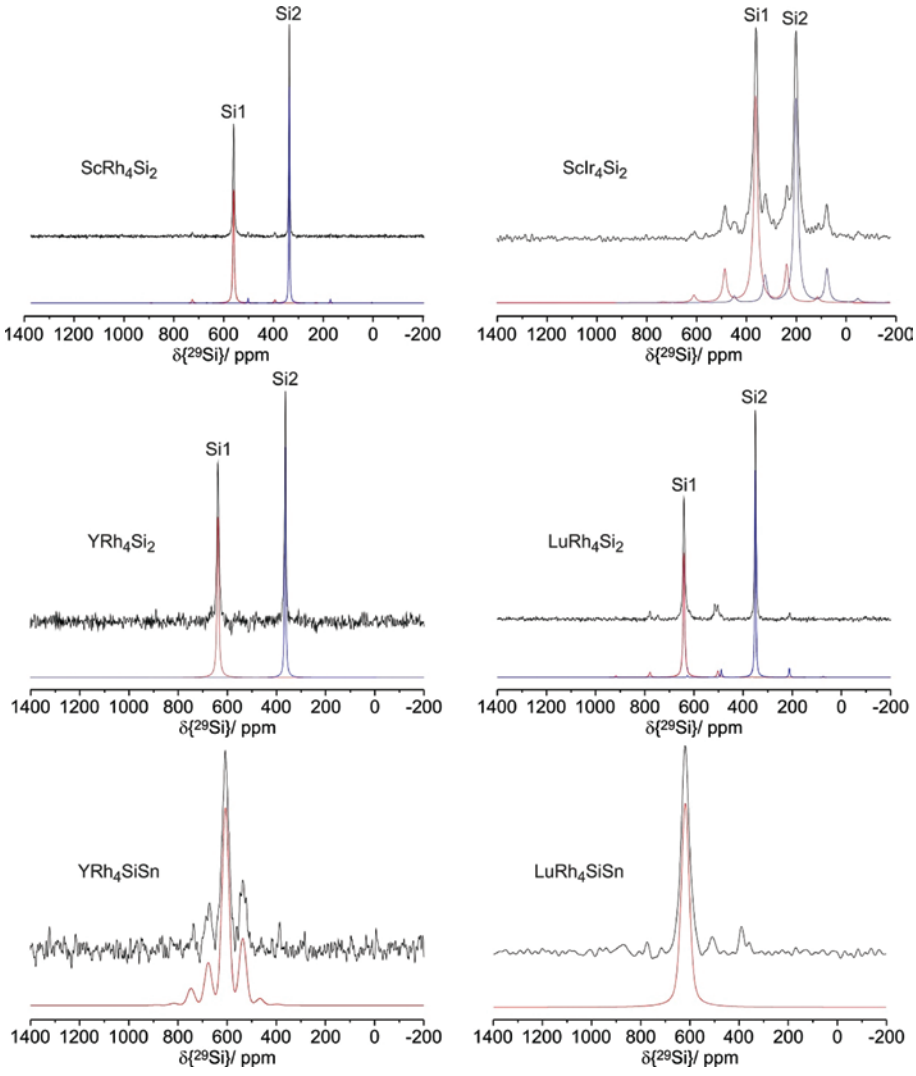


**Fig. 6:** $^{29}$Si solid state MAS NMR spectra of $ScRh_4Si_2$, $ScIr_4Si_2$ (top), $YRh_4Si_2$, $LuRh_4Si_2$ (middle), $YRh_4SiSn$ and $LuRh_4SiSn$ (bottom) recorded at 9.4 T along with simulations (colored lines). Minor peaks are spinning sidebands.

single signals, which hence must be attributed to the Si1 sites. Compared to those of the ternary compounds these signals are strongly broadened, which can be attributed to the structural and electronic disorder effects introduced by the tin substitution on the Si2 site.

Figures 7 and 8 show the $^{45}$Sc and $^{89}$Y MAS-NMR spectra of $ScRh_4Si_2$, $ScIr_4Si_2$, $YRh_4Si_2$ and $YRh_4Ge_2$, confirming the presence of unique crystallographic sites for the rare-earth species. The $^{45}$Sc spectra show wide spinning sideband manifolds originating from the outer $\pm1/2 \leftrightarrow \pm3/2$, $\pm3/2 \leftrightarrow \pm5/2$, and $\pm5/2 \leftrightarrow \pm7/2$ Zeeman-transitions, which are anisotropically shifted by first- and second-order quadrupolar perturbations. In addition, the central resonances show a characteristic shape from second-order quadrupolar perturbation effects, allowing the determination of the quadrupolar coupling constant $C_Q$ and the asymmetry parameter $\eta_Q$ from simulation. In the case of $ScRh_4Si_2$ the line shape of the target compound could only be simulated by including a second signal contribution (fractional area 18 %), whose line shape was approximated by a Gaussian. Consistent simulations at two different magnetic field strengths show that the position of this extra component (1188 ppm at 4.7 T and 1241 ppm at 11.7 T) is influenced by second-order quadrupolar shifts, and its full width at half maximum (7053 Hz at 4.7 T and 2630 Hz at 11.7 T) is dominated by this mechanism. We attribute this extra line shape component to an impurity.

The $^{89}$Y MAS-NMR signals show spinning sideband patterns with asymmetric intensity distributions, reflecting a Knight Shift anisotropy, in accordance with the non-cubic structural environment of the $^{89}$Y atoms. All the NMR

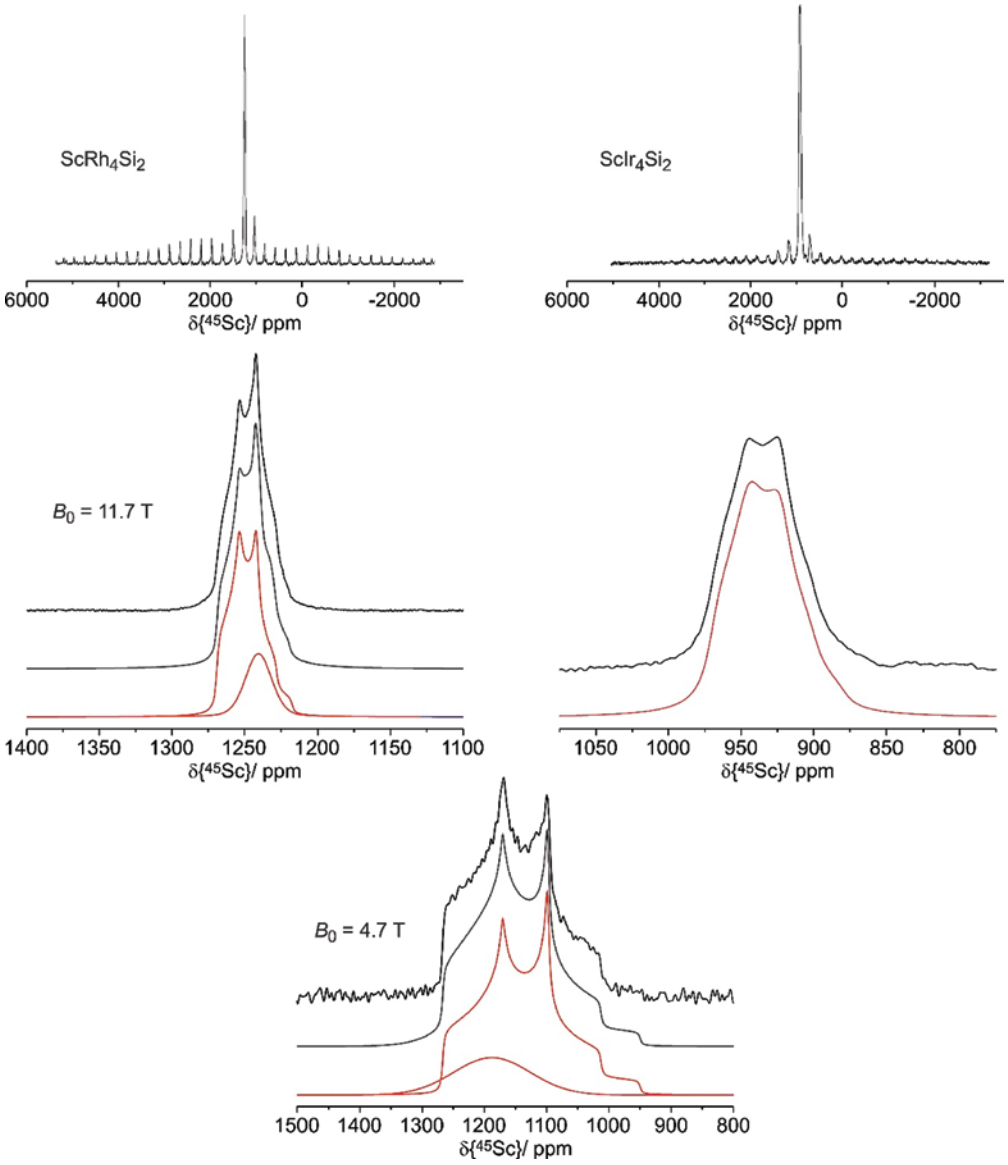


**Fig. 7:** Top: $^{45}Sc$ solid state MAS NMR spectra of $ScRh_4Si_2$ and $ScIr_4Si_2$. Minor peaks are spinning sidebands. Middle: horizontal expansion of the $^{45}Sc$ MAS center bands at 11.7 T, including simulations. In the case of $ScRh_4Si_2$ the fit requires inclusion of an additional Gaussian line shape component, attributed to an impurity. Bottom: expanded $^{45}Sc$ spectrum of $ScRh_4Si_2$ recorded at an external magnetic flux density of $B_0 = 4.7$ T, including the simulations.

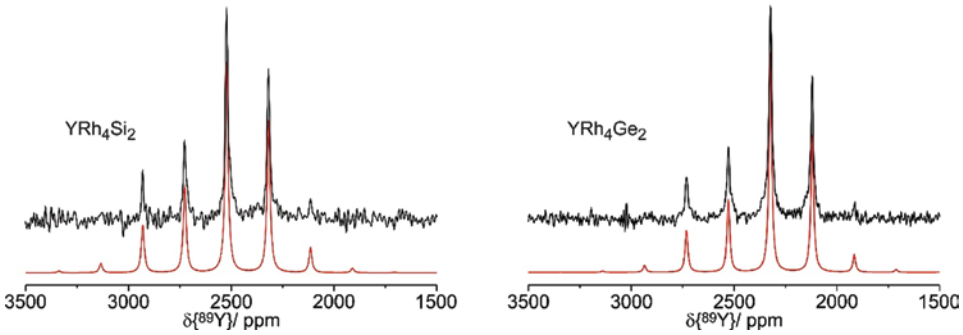


**Fig. 8:** $^{89}Y$ MAS-NMR spectra of $YRh_4Si_2$ and $YRh_4Ge_2$ recorded at 11.7 T along with simulations (colored lines). The spinning sideband patterns arise from the Knight Shift anisotropy.

**Tab. 8:** $^{29}Si$, $^{45}Sc$ and $^{89}Y$ NMR parameters of the silicides $RET_4Si_2$, $RET_4SiSn$ and the germanide $YRh_4Ge_2$: isotropic resonance shifts $\delta_{iso}$ (±1/ppm); full width at half maximum (FWHM ± 0.01/kHz), degree of Gaussian (G) vs. Lorentzian (L) character of the central signal, magnetic shielding anisotropy $\delta_K$ (±1/ppm), asymmetry parameter $\eta_K$, 90° pulse length $p_1$ (/μs), relaxation delay $d_1$ (/s), magnetic flux density of external magnetic field $B_0$ (/T), spinning frequency (/kHz), quadrupolar coupling constant $C_Q$ (/MHz) and electric field gradient asymmetry parameter $\eta_{CQ}$.

| | Site | $\delta_{iso}$ | FWHM | G/L | $\delta_K$ | $\eta_K$ | $p_1$ | $d_1$ | $B_0$ | $\nu_{rot}$ |
|---|---|---|---|---|---|---|---|---|---|---|
| $ScRh_4Si_2$ | | | | | | | | | | |
| $^{29}Si$ | Si1 | 574 | 0.39 | 0.16 | 105 | 0.66 | 5.5 | 1.0 | 7.05 | 10 |
| | Si2 | 348 | 0.18 | 0 | 92 | 0.02 | | | | |
| $ScIr_4Si_2$ | | | | | | | | | | |
| $^{29}Si$ | Si1 | 347 | 1.45 | 0 | 173 | 0.78 | 4.5 | 1.0 | 9.4 | 10 |
| | Si2 | 183 | 1.46 | 0 | 167 | 0.63 | | | | |
| $YRh_4Si_2$ | | | | | | | | | | |
| $^{29}Si$ | Si1 | 637 | 0.64 | 0 | – | – | 5.0 | 1.0 | 9.4 | 10 |
| | Si2 | 363 | 0.39 | 0 | – | – | | | | |
| $^{89}Y$ | | 2522 | 0.42 | 0 | 504 | 0.47 | 17.5 | 0.5 | 11.7 | 5 |
| $YRh_4Ge_2$ | | | | | | | | | | |
| $^{89}Y$ | | 2324 | 0.39 | 0 | 477 | 0.31 | 17.5 | 0.5 | 11.7 | 5 |
| $LuRh_4Si_2$ | | | | | | | | | | |
| $^{29}Si$ | Si1 | 641 | 0.64 | 0 | 125 | 0.04 | 4.5 | 1.0 | 9.4 | 11 |
| | Si2 | 350 | 0.41 | 0.11 | 100 | 0.06 | | | | |
| $YRh_4SiSn$ | | | | | | | | | | |
| $^{29}Si$ | | 607 | 2.66 | 0.91 | 128 | 0.36 | 5.0 | 1.0 | 9.4 | 6 |
| $LuRh_4SiSn$ | | | | | | | | | | |
| $^{29}Si$ | | 619 | 3.08 | 0.53 | – | – | 4.5 | 1.0 | 9.4 | 10 |
| | | $\delta_{iso}$ | FWHM | G/L | $C_Q$ | $\eta_Q$ | $p_1$ | $d_1$ | $B_0$ | $\nu_{rot}$ |
| $ScRh_4Si_2$ | | | | | | | | | | |
| $^{45}Sc$ | | 1271 | – | – | 1.09 | 0.53 | 0.83 | 0.5 | 11.7 | 28 |
| | | 1277 | – | – | 1.08 | 0.53 | 0.76 | 0.25 | 4.7 | 28 |
| $ScIr_4Si_2$ | | | | | | | | | | |
| $^{45}Sc$ | | 974 | – | – | 1.45 | 0.5 | 0.93 | 0.25 | 11.7 | 28 |

parameters deduced from these spectra are summarized in Table 8. In accordance with our previously published results for other series of isotypical compounds, the $^{89}Y$ Knight Shift difference between $YRh_4Si_2$ and $YRh_4Ge_2$ can be related to the electronegativity of the tetrel group element [29–32].

Our attempts of obtaining the $^{119}Sn$ NMR signal of $YRh_4SiSn$ were unsuccessful, while in the case of $LuRh_4SiSn$ an extremely broad resonance within the frequency range 1750–2550 ppm was observed (data not shown). We conclude that the structural and electronic disorder caused Si/Sn mixing in the structure leads to a wide distribution of Knight Shifts, sabotaging the observation of interpretable signals.

**Acknowledgments:** We thank Dipl.-Ing. U. Ch. Rodewald for collection of the single crystal diffractometer data. Support by the Deutsche Forschungsgemeinschaft is gratefully acknowledged.

# References

[1] P. Villars, K. Cenzual, Pearson's Crystal Data: Crystal Structure Database for Inorganic Compounds (release 2015/16), ASM International®, Materials Park, Ohio (USA), **2015**.
[2] G. Knebel, C. Eggert, D. Engelmann, R. Viana, A. Krimmel, M. Dressel, A. Loidl, *Phys. Rev. B* **1996**, *53*, 11586.
[3] S. Tuncel, R.-D. Hoffmann, R. Pöttgen, *Z. Anorg. Allg. Chem.* **2007**, *633*, 986.
[4] J. T. Zhao, E. Parthé, *Acta Crystallogr. C* **1990**, *46*, 2273.
[5] M. Chondroudi, M. Balasubramanian, U. Welp, W.-K. Kwok, M. G. Kanatzidis, *Chem. Mater.* **2007**, *19*, 4769.
[6] A. Oliynyk, S. S. Stoyko, A. Mar, *Inorg. Chem.* **2013**, *52*, 8264.
[7] D. Voßwinkel, O. Niehaus, B. Gerke, C. Benndorf, H. Eckert, R. Pöttgen, *Z. Anorg. Allg. Chem.* **2015**, *641*, 238.
[8] D. Voßwinkel, S. F. Matar, R. Pöttgen, *Monatsh. Chem.* **2015**, *146*, 1375.
[9] R. Pöttgen, Th. Gulden, A. Simon, *GIT Labor-Fachzeitschrift* **1999**, *43*, 133.
[10] A. V. Morozkin, Yu. D. Seropegin, O. I. Bodak, *J. Alloys Compd.* **1996**, *234*, 143.

[11] A. V. Morozkin, Yu. D. Seropegin, *J. Alloys Compd*. **1996**, *237*, 124.
[12] A. V. Morozkin, Yu. D. Seropegin, I. A. Sviridov, O. I. Bodak, *J. Alloys Compd*. **1998**, *274*, L1.
[13] W. Jeitschko, E. J. Reinbold, *Z. Naturforsch*. **1985**, *40b*, 900.
[14] K. Yvon, W. Jeitschko, E. Parthé, *J. Appl. Crystallogr*. **1977**, *10*, 73.
[15] W. Kohn, L. J. Sham, *Phys. Rev*. **1965**, *140*, A1133.
[16] P. Hohenberg, W. Kohn, *Phys. Rev*. **1965**, *136*, B864.
[17] A. R. Williams, J. Kübler, C. D. Gelatt Jr., *Phys. Rev. B* **1979**, *19*, 6094.
[18] V. Eyert, *Int. J. Quantum Chem*. **2000**, *77*, 1007.
[19] J. P. Perdew, K. Burke, M. Ernzerhof, *Phys. Rev. Lett*. **1996**, *77*, 3865.
[20] P. E. Blöchl, *Phys. Rev. B* **1994**, *50*, 17953.
[21] R. Hoffmann, *Angew. Chem. Int. Ed. Engl*. **1987**, *26*, 846.
[22] Bruker Corp., Topspin (Version 2.1), Karlsruhe, Germany, **2008**.
[23] D. Massiot, F. Fayon, M. Capron, I. King, S. Le Calvé, B. Alonso, J.-O. Durand, B. Bujoli, Z. Gan, G. Hoatson, *Magn. Reson. Chem*. **2002**, *40*, 70.
[24] V. Petříček, M. Dušek, L. Palatinus, *Z. Kristallogr.* **2014**, *229*, 345.
[25] E. Parthé, L. Gelato, B. Chabot, M. Penzo, K. Cenzual, R. Gladyshevskii, TYPIX–*Standardized Data and Crystal Chemical Characterization of Inorganic Structure Types*. Gmelin Handbook of Inorganic and Organometallic Chemistry, 8th edition, Springer, Berlin (Germany), **1993**.
[26] J. Emsley, *The Elements*, Oxford University Press, Oxford (U.K.), **1999**.
[27] J. Donohue, *The Structures of the Elements,* Wiley, New York, **1974**.
[28] R. Pöttgen, *Z. Naturforsch*. **2006**, *61b*, 677.
[29] C. Benndorf, O. Niehaus, H. Eckert, O. Janka, *Z. Anorg. Allg. Chem*. **2015**, *641*, 168.
[30] M. Johnscher, S. Stein, O. Niehaus, C. Benndorf, L. Heletta, M. Kersting, C. Höting, H. Eckert, R. Pöttgen, *Solid State Sci*. **2016**, *52*, 57.
[31] T. Harmening, H. Eckert, C. M. Fehse, C. P. Sebastian, R. Pöttgen, *J. Solid State Chem*. **2011**, *184*, 3303.
[32] C. Benndorf, H. Eckert, R. Pöttgen, *Dalton Trans.* **2016**, *45*, 8215.